Scanning Small-Angle X-ray Scattering of Injection-Molded Polymers: Anisotropic Structure and Mechanical Properties of Low-Density

ACS APPLIED POLYMER MATERIALS

pubs.acs.org/acsapm

Article

Scanning Small-Angle X-ray Scattering of Injection-Molded Polymers: Anisotropic Structure and Mechanical Properties of Low-Density Polyethylene

Linnea Björn, Renan Melhado Mazza, Eskil Andreasson, Fredrik Linell, Viviane Lutz-Bueno, Manuel Guizar-Sicairos, Elin Persson Jutemar, and Marianne Liebi*

Cite This: https://doi.org/10.1021/acsapm.3c01007

Read Online

ACCESS | Metrics & More | Article Recommendations | Supporting Information

ABSTRACT: Injection molding is known to create a layered anisotropic morphology across the sample thickness due to varying shear and cooling rates during the manufacturing process. In this study, scanning small-angle X-ray scattering was used to visualize and quantify the distribution of hierarchical structures present in injection-molded parts of low-density polyethylene (LDPE) with varying viscosities. By combining scattering data with results from injection molding simulations and tensile testing, we find that oriented shish-kebab structures, as well as elongated spherulite structures consisting of semicrystalline ellipsoids, contribute to high ultimate tensile strength along the flow direction. Furthermore, we show that a higher degree of orientation is found close to the injection gate and in LDPE with higher viscosity, consequently from elevated shear and cooling rates present during the injection molding process.

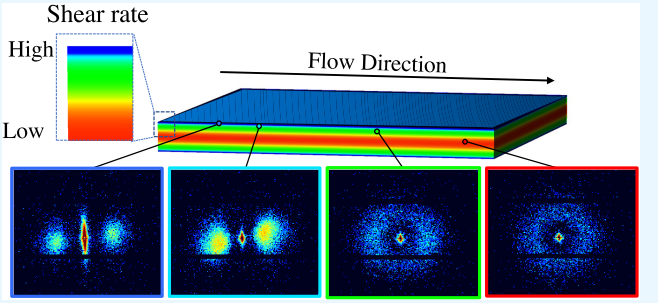

KEYWORDS: *polyethylene, scanning SAXS, mechanical performance, morphology, computational modeling*

INTRODUCTION

Injection-molded semicrystalline polymers are widely used in commercial applications due to their beneficial mechanical properties, light weight, high flexibility, and low price. During the injection molding process, the polymer is heated until melted and injected at a high flow rate and pressure into a cool mold. During the process, the polymer is subjected to high shear flow as well as fast cooling rates, which impacts its crystalline structure. The injection molding process is often used to produce products with complex three-dimensional (3D) shapes, which results in varying local process conditions throughout the product. Consequently, the polymer morphology will differ along the product, giving rise to varying mechanical performance. Understanding the correlation between processing conditions, resulting morphology, and mechanical performance is essential to produce high-quality injection-molded products.

Injection-molded parts are known to create a multiphase layer through the thickness, adding to the complexity of the morphology. Kantz et al. used optical microscopy and X-ray diffraction to show a layered structure of injection-molded polypropylene consisting of clearly defined skin, shear, and bulk layers.[1] It was also shown that some layers appeared isotropic when viewed perpendicular to the flow, while a high degree of orientation was seen when viewed parallel to the flow, motivating the investigation of multiple directions. Schrauwen et al. also used optical microscopy in combination with X-ray scattering to visualize a multiphased layered structure in injection-molded high-density polyethylene (HDPE) consisting of a skin layer, transition layer, shear layer, fine-grained layer, and bulk layer. Mechanical properties such as impact toughness were then associated with the crystalline orientation.[2]

Several studies have been using small- and wide-angle X-ray scattering (SAXS/WAXS),[3] often in combination with other techniques such as scanning electron microscopy (SEM),[4] differential scanning calorimetry (DSC),[5] and mechanical testing[6,7] or a combination of them[8] in order to get an in-depth understanding of the hierarchical structures in injection-molded polymers. It has been shown that the skin layers, where the shear and cooling rates are high, often consist of so-called shish-kebab structures. These structures are thread-like, highly oriented parallel to the flow direction, and have crystalline lamellae growing perpendicular to the flow direction.[9] Close to the central line of the mold, both the shear rate and

Received: May 16, 2023
Accepted: June 29, 2023

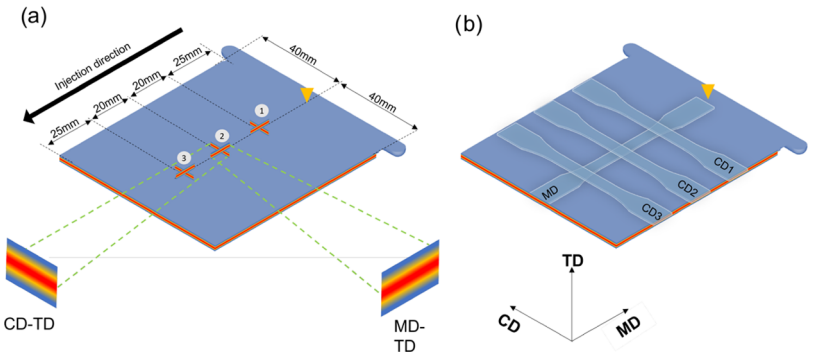

Figure 1. Injection-molded test plate with dimensions and positions of the measured samples. The yellow triangles correspond to the injection gate. (a) Preparation of the cross section in CD−TD and MD−TD cutting planes, which were used to study the layered structure along the plate thickness direction (TD). (b) Geometry, directions, and positions for punching of dogbones in MD, CD1, CD2, and CD3, which were used for mechanical tests and scanning SAXS experiments of deformed samples.

temperature gradient will be low, resulting in randomly oriented polymer chains in symmetrical spherulites.[10]

The structure of the injected semicrystalline polymer is not only dependent on processing conditions but also on the molecular architecture of the polymer.[11] Depending on the intrinsic nature of the monomers and varying polymerization parameters, different branching degrees of the polymer chains are possible. Increasing the number of branching points reduces the ability of the polymer molecule to arrange and relax at short distances, forming crystals, and reducing the crystallinity, hence the density of the polymer.[12] A high degree of crystallinity is associated with high stiffness, tensile strength, and hardness.

In addition, molecular weight and molecular weight distribution of polymers are also reported to affect the injection-molded structures.[13−15] An example is the study made by Cao et al.,[16] who showed that the overall orientation in injection-molded samples is elevated with increased molecular weight. This elevation is explained by the assumption that polymer chains with high molecular weights are more easily oriented by the flow direction than polymers with lower molecular weights. However, other studies have also shown that a high degree of orientation was formed in samples with lower molecular weights rather than higher ones. An example is a study of injection-molded HDPE carried out by Liu et al.[17] This study explained the phenomena with the assumption that the higher viscosity in HDPE with a higher molecular weight generated a lower shear rate and thus a lower orientation. In short, how the molecular weight affects the microstructure of injection molding polymers is an ongoing debate.

A common approach to linking material properties to processing conditions is the use of numerical simulations. Simulation programs have been used to model the injection molding process, providing a better understanding of the injection molding optimization parameters and the properties of the molded test object. In 1978, Tan et al.[18] published the use of mathematical models predicting the amounts of flow-induced crystallization in injection-molded HDPE. Following this pioneer study, simulations have been widely used to describe the mold elasticity effect on holding pressure mold shrinkage (Leo et al.[19]) and to predict flow-induced crystallization kinetic, anisotropic properties of isotactic polypropylene (Zheng et al.[20]). Similarly, recent work on microinjection molding (MIM) has shown that simulations can be used to characterize a wide variety of parameters, such as the injection speed profile, pressure at injection point, melt and mold temperatures, 3D mesh parameters, and material rheological characterization (Tosello et al.[21]), but also to describe the thermomechanical history experienced by polymer chains during MIM and to make crystallization models to describe the two morphologies of spherulites and fibrils (Speranza et al.[22]). However, due to the complexity of the process, the large quantity of fitting parameters and of processes involved in polymer injection molding, linking simulation models to experimental characterization can be challenging.

Despite the advances in understanding the relationship between the structure and mechanical properties of injection-molded polymers, commercial applications still often rely on trial and error to achieve the desired material performance, often resulting in a costly process design. This study aims to shed light on how synchrotron scanning small-angle X-ray scattering (SAXS) can be used to capture the multiphase structures through the thickness of injection-molded low-density polyethylene (LDPE) with a high degree of long chain branching and varying molecular weights. Special attention was given to probing structural variations throughout the sample thickness. Furthermore, to understand and compare structures in the semicrystalline polymer studied, the scanning SAXS data were compared with numerical simulations, mechanical testing, and thermal analysis.

EXPERIMENTAL SECTION

Materials. Two types of LDPEs from Ineos [Brussels, Belgium] were compared. The first LDPE had a melt flow index (MFI) of 22 g/10 min (190 °C, 2.16 kg) and a density of 0.923 g/cm^3 and will hereafter be designated as medium-viscosity LDPE. The second LDPE had an MFI of 55 g/10 min (190 °C, 2.16 kg) and a density of 0.923 g/cm^3 and will hereafter be designed as low-viscosity LDPE.

Injection Molding and Sample Preparation. A hydraulic injection molding machine (Arburg 470 800-70S, Arburg GmbH Germany) was used to produce test plates with a thickness of 0.6 mm, following ISO 294-5. Briefly, the plastic melt was injected at a temperature of 220 °C and a volume flow of 20 cm^3/s into a mold with a temperature of 40 °C. The maximum pressure reached during injection was 1490 bars for medium-viscosity LDPE and 1170 bars for low-viscosity LDPE. At 99% filling degree, the volume-controlled filling was switched to pressure-controlled during the holding pressure phase, and the holding pressure was adjusted to obtain plates with a thickness of 0.6 mm. For medium-viscosity LDPE, the holding pressure was decreased from 900 to 750 bars for 0.3 s, followed by a

https://doi.org/10.1021/acsapm.3c01007
ACS Appl. Polym. Mater. XXXX, XXX, XXX−XXX

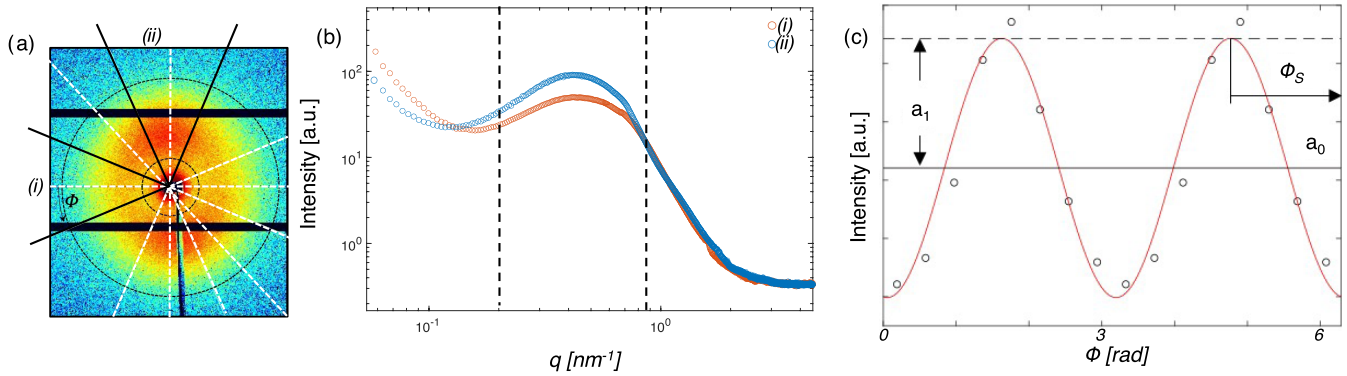

Figure 2. SAXS 2D pattern (a) and integrated intensity (b) of medium-viscosity LDPE. The radial integration is performed in horizontal (i) and vertical azimuthal segments (ii). (c) Azimuthally integrated intensity capturing the asymmetry of the scattering pattern in the q-range from 0.26 to 0.94 nm^{-1}, as indicated with dashed lines in panel (b).

decrease to 500 bars for 0.3 s. The corresponding pressures and times for low-viscosity LDPE were 800 bar − 0.3 s − 650 bar − 0.3 s − 450 bars. After the release of the hold pressure, the plates were cooled for 11 s. The fixed mold half was made from steel DIN 45 NiCrMo 16, while the moving half plate was made from the high-strength aluminum−zinc alloy AlZnMgCU 1,5. The mold was equipped with a floodgate to ensure that the flow front evolves evenly in the plate; see Figure S1.

For scanning SAXS, cross sections were sliced along two cutting planes to capture two perpendicular two-dimensional (2D) projections (CD−TD and MD−TD) of the structures at three positions on the plate (Figure 1a). The cross sections were prepared to study structural changes in the thickness direction (TD), where samples were prepared either in the machine direction (MD) parallel to the flow or in the cross direction (CD) perpendicular to the flow, resulting in the MD−TD and CD−TD viewing planes. The samples were prepared by cutting slices of thickness 50 μm by using a microtome (Leica RM2255 from Triolab). Note that samples for CD−TD and MD−TD planes were cut from separate plates. The size in the TD direction of the injection-molded plates varied between 0.592 and 0.600 mm, and to directly compare the layer distributions, a normalized plate thickness was used.

Test samples in the shape of dogbones, following ISO 527-2 1BA, were punched out mechanically from the test plates. Dogbones in machine direction (MD) were punched in the plastic flow direction in the center of the plate. Dogbones in the cross direction (CD) were punched perpendicular to the plastic flow direction in three different positions on the plate (Figure 1b).

Scanning SAXS analysis was also used for deformed dogbones after mechanical testing. For these measurements, cross sections were prepared in two planes/viewing directions. Dogbones in the top view were viewed through the full thickness of the dogbone in the CD−MD plane, while samples from deformed dogbones in the side view were prepared by preparing thin slices by means of a scalpel to view the cross sections in CD−TD and MD−TD planes, respectively.

Scanning SAXS. All scanning SAXS experiments were performed at the cSAXS beamline X12SA of the Swiss Light Source, Paul Scherrer Institute, Switzerland. The X-ray energy was set to 11.2 keV with a fixed-exit double-crystal Si(111) monochromator. The beam was focused horizontally by bending the second monochromator crystal and vertically by bending an Rh-coated mirror. Two different measuring configurations were used. The first experimental configuration, used for cross section samples from the injection-molded plate, had a beam size of 7.5 × 28 μm (see Figure S11), a step size of 10 × 25 μm, and an exposure time of 0.1 s per scattering pattern. A Pilatus 2M detector[23] was placed at a distance of 2.183 m from the samples with a flight tube under vacuum placed in-between to reduce air scattering and X-ray absorption. A 1.5 mm steel beamstop placed inside the evacuated flight tube blocked the direct beam; the X-ray fluorescence from the beamstop is proportional to the incoming X-ray intensity and was recorded with a CyberStar (Oxford Danfysik) detector. The goal of this setup was to obtain a small beam in the vertical direction to optimize the resolution along the plate thickness.

For the second experimental configuration, the main goal was to probe the larger areas of the deformed dogbone samples. Therefore, the beam dimensions were increased to 40 × 40 μm and the step size of 40 × 40 μm for dogbones measured in the side view (across CD−TD or MD−TD cutting planes) and 60 × 60 μm for dogbones measured in the top view (across CD−MD cutting plane). The exposure time per scattering pattern was 0.1 s, and the distance between the Pilatus 2M detector and the samples was 2.167 m. The transmitted beam was measured with a photodiode on the beamstop placed inside the flight tube.

The 2D scattering patterns were azimuthally integrated into 16 angular segments, and the orientation and the degree of orientation were analyzed in specific q-ranges according to Bunk et al.[24] and are shown in Figure 2. The samples consisting of cross sections in CD−TD and MD−TD planes were studied using two different q-regions of the SAXS signal. The first region, q = 0.26−0.94 nm^{-1}, includes a scattering peak, which quantifies the main repetition period of the sample. For LDPE, the scattering peak originates from the lamellae spacing (d_{ac}). This q-region is located within the dashed lines in Figure 2b. The second q-region, q = 0.01−0.17 nm^{-1}, represents the scattering at lower q. Moreover, a q-region of 0.31−0.84 nm^{-1} was used to perform a peak-fitting analysis, which is described in more detail below.

For the analysis of the deformed samples after the fracture, a q-region of 0.21−0.90 nm^{-1} was used for the analysis of the degree of orientation and asymmetric intensity, whereas q = 0.22−1.89 nm^{-1} was used for the peak fitting.

Each scattering pattern results in an average intensity contribution a_0 given by the average scattering, an asymmetric intensity contribution a_1 given by the anisotropic scattering, and a direction of orientation Φ_S given by the highest scattering intensity. The degree of orientation is here defined as the ratio a_1/a_0.[2424] For deformed samples measured after the fracture, plots combining the orientation and asymmetric intensity in HSV color-coding were used. In these figures, the hue corresponds to the orientation angle of the scattering, whereas the asymmetric scattering corresponds to the value of the color.

For performing peak-fitting analysis, transmission and Lorentz-corrected azimuthally integrated data averaged over all azimuthal segments were used. The scattering signal in this q-range can be decomposed into the sum of a power law decay and a peak; see Figure S2. Before and after the peak, the power law decay was fitted with a negative exponential and subtracted from the whole range data. This was done for the ranges q = 0.25−0.29 and 0.86−0.89 nm^{-1} for undeformed cross sections and q = 0.17−0.20 and 1.91−1.94 nm^{-1} for the deformed samples. A Gaussian function was then used to fit the remaining data, from which the peak position and full-width half

https://doi.org/10.1021/acsapm.3c01007
ACS Appl. Polym. Mater. XXXX, XXX, XXX−XXX

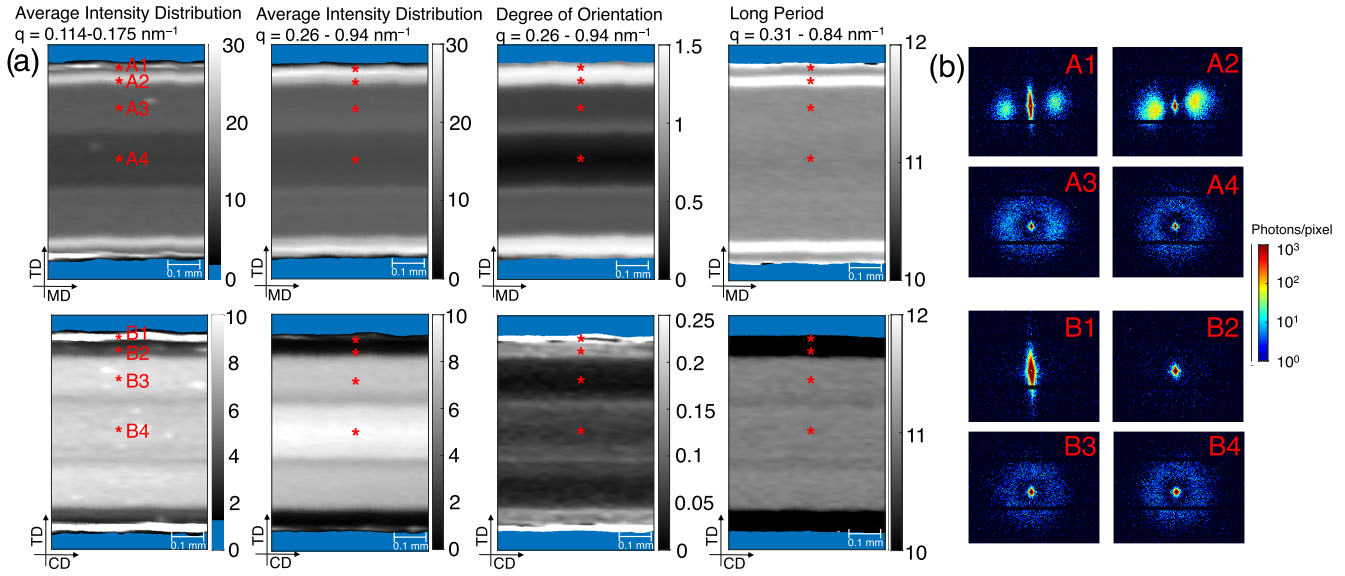

Figure 3. Average intensity contribution, the degree of orientation, and the calculated long period from the center of the plate for cross sections of medium-viscosity LDPE, perpendicular (CD−TD plane) and parallel (MD−TD plane) to the flow (a), as well as scattering patterns from selected points A1-4 and B1-4 along the plate thickness (b). Note that the scale of the color bar differs between MD−TD and CD−TD, as the intensity and the degree of orientation, respectively, differed significantly. Blue represents the masked area outside the sample.

maxima could be obtained. The long period was calculated from the $2*\pi$/peak position.

Correlation Function Analysis. To determine the lamellae thickness and crystallinity, we analyzed the correlation function.[25,26] The analysis was done in SasView, where the one-dimensional (1D) correlation function was defined as

$$K(z) = \frac{1}{Q}\int_0^\infty I(q)q^2\cos(qz)\mathrm{d}q \tag{1}$$

where Q is the Porod invariant. The data were extrapolated to $q = 0$ by using a Guinier function to fit the data in the low q-range

$$I(q) = A\ \mathrm{e}^{Bq^2} \tag{2}$$

whereas a Porod function was used to extrapolate the data to $q = \infty$ to fit the data in the high q-range

$$I(q) = Kq^{-4}\ \mathrm{e}^{-q^2\sigma^2} + Bg \tag{3}$$

From the analysis, an estimation of the lamellae thickness was taken as the linear extrapolation in the initial portion of the correlation function curve with the horizontal line tangent to the first minimum peak, as described in Figure S3. The correlation function analysis assumes isotropic scattering; therefore, the 2D scattering patterns were split into 16 azimuthal cakes, and only the scattering directions with the most prominent lamellae scattering signals were used for the analysis. Thereby, horizontal scattering was used for the MD−TD, and vertical scattering direction was used for the CD−TD.

A statistical evaluation of the outcome of the correlation function analysis was performed to determine which factors had a statistically significant effect on the different variables. The included factors were the cutting plane, the LDPE viscosity, the through-thickness layer, and the spatial position on the plate, while the variables studied were the crystallinity, the lamella thickness, and the long period. A commercial software, Minitab 18, was used to perform a multivariate analysis of variance (MANOVA) test by fitting a general linear model combined with a Tukey post-hoc comparison using a 95% confidence interval.

Thermal Analysis. A standard DSC equipment, DSC 3+ [Mettler Toledo, Switzerland], was used to perform thermal tests on specimens from injection-molded plates produced by medium-viscosity LDPE and low-viscosity LDPE. Circular-shaped specimens were punched from positions 1, 2, and 3, respectively, with an approximate sample weight of 8 mg, and placed in 20 μL of aluminum crucibles. The first melting was analyzed under heating at 10 °C/min in a nitrogen gas environment.

Mechanical Testing. A standard tensile test equipment Zwick Z010 Proline [ZwickRoell, Germany], with a load cell of 1 kN, was used to perform tensile tests on the dogbones. The tests were performed at room temperature under displacement control, with a loading rate of 100 mm/min and a gauge length between the grips of 58 mm. A total of 10 samples were measured for each material, and the results were averaged to obtain the stress−strain curve.

Simulation. A commercial software, Autodesk Moldflow Insight 2019, was used to perform a finite element simulation of the injection molding process. A 3D tetrahedral-shaped mesh with 1640624 elements distributed in 20 layers through the thickness was used. A graphical representation of the simulation model, including the 3D mesh density, can be found in the Supporting Information; see Figure S1. The process settings (boundary conditions) were the same values used in the injection molding process during the sample preparation. The polymer material viscosity is described by the Cross-WLF material model[27] using the material coefficient presented in Table S1. The model uses the conservation equations of momentum, mass, and energy to characterize the flow field. A finite element method is used to solve the equations and obtain the velocity, pressure, and temperature field.

Conservation of mass for a fluid

$$\frac{\delta\rho}{\delta t} + \nabla\cdot(\rho\cdot V) = 0 \tag{4}$$

where

- ρ is the polymer density
- t is the time
- V is the velocity vector

Conservation of momentum

$$\rho\frac{DV}{Dt} = -\nabla P + \nabla\cdot\tau + \rho g \tag{5}$$

- P is the pressure
- τ is the viscous stress tensor
- g is the gravitational acceleration vector

Conservation of energy

https://doi.org/10.1021/acsapm.3c01007
ACS Appl. Polym. Mater. XXXX, XXX, XXX−XXX

$$\rho c_p \frac{DT}{Dt} = \nabla \cdot (k \nabla T) + \tau : \nabla \vee + \beta T \frac{DP}{Dt} \quad (6)$$

- k is the polymer thermal conductivity
- c_p is the specific heat capacity of the melt
- β is the polymer expansivity, which is defined as follows:

$$\beta = -\frac{1}{\rho} \cdot \frac{\delta \rho}{\delta T} \quad (7)$$

For evaluating the simulation results, a compilation was done by grouping the pictures from a specific field (e.g., shear rate or temperature) for several time steps, as demonstrated in Figure S4 in the Supporting Information.

RESULTS AND DISCUSSION

In order to evaluate the anisotropic structure of the layers, scanning SAXS was performed in the center of the plate in the two orthogonal cutting planes, MD−TD and CD−TD (according to Figure 1a). The results are presented in Figure 3, where four distinctive layers were revealed in the average intensity contribution, the degree of orientation, and the long-distance spacing plots according to points A1-4 and B1-4. The average intensity contribution corresponds to the average scattering in the specified q-region, whereas the degree of orientation corresponds to the orientation of the scattering pattern, and both can be used to determine regions in the samples where the scattering behavior changes. However, to determine the structure present, the 2D scattering patterns should be evaluated.

The first layer closest to the mold (A1) shows a high degree of orientation and average intensity contribution, and scattering patterns A1 and B1 show that the layer consists of a highly oriented structure visible in both cutting planes. In this layer, the peak fitting in the MD−TD plane of the Lorentz-corrected data gives a long-distance period of around 11.3 nm. The CD−TD scattering pattern consists of a single narrow vertical streak, whereas the MD−TD plane is characterized by a similar vertical streak and a two-point pattern in the horizontal direction. These scattering patterns are characteristic of a shish-kebab structure.[9,28,29]

Since this layer is close to the edge of the sample, the sharp vertical streak observed can contain contributions from the sample−air interface (see Figure S12). Note that the long period could not be calculated in this layer in the CD−TD plane since there was no lamellae peak present. The first and second layers can clearly be distinguishable from each other in the degree of orientation in the CD−TD plane and average intensity contribution in both cutting planes at low q, whereas the values extracted from the q-range 0.26 to 0.94 nm^{-1} are similar for layers 1 and 2. Note that the degree of orientation in CD−TD from scattering patterns B1 and B2 is based on the contribution of the vertical streak only since no contribution from the lamellae was present in the CD−TD projection. The clear difference at low q arises due to the fact that in layer 1, the scattering is dominated by the vertical streak, whereas in layer 2, the scattering is dominated by the two-point pattern. Compared to layer 1, the long-distance period in layer 2 is significantly larger, around 12.4 nm. Comparing the scattering patterns A1 and A2, it can be seen that the vertical streak is clearly reduced in layer 2 compared to layer 1, while the two-point pattern, characteristic of the lamellae, becomes more intense in layer 2. This indicates that there are fewer fiber-like shish structures present in the second layer. For a more in-depth distinction between the different oriented morphologies in the first and second layers, the SAXS data would need complementation of full azimuthal WAXS data, which was not available in the setup used for this study.

In the third and fourth layers of the sample, the scattering patterns are less anisotropic, as shown by the degree of orientation and scattering patterns A3-A4 and B3-B4, respectively. The long period is similar for both layers 3 and 4, around 11.1 nm. A single diffuse circular scattering pattern with no preferred orientation found in A4 and B4 is associated with the spherulite microstructure. However, in the third layer in the MD−TD plane, the scattering pattern A3 shows a slight orientation in the horizontal direction, whereas in the CD−TD plane, the scattering pattern B3 is isotropic. Such scattering patterns, in combination with the lower degree of orientation, are consistent with elongated spherulites with the long axis oriented in the flow direction and lamellae preferentially directed perpendicular to the flow as the microstructure suggested by Katti and Schultz.[30]

The first and second layers consisting of highly oriented structures will from here on be referred to as "skin layer 1" and "skin layer 2," while the third layer consisting of elongated spherulites will be referred to as the "shear layer" and the fourth layer consisting of symmetric spherulites will be referred to as the "bulk layer." Azimuthally integrated intensity for the four layers is shown in the Supporting Information (Figure S8).

In order to examine the influence of the molecular weight of a polymer on the layered structure through the plate thickness, two LDPEs with different viscosities were measured. The degree of orientation (based on the q-range of 0.26−0.94 nm^{-1}) in both MD−TD and CD−TD planes was calculated and plotted as a function of the normalized thickness of the cross section for three different positions of the injection-molded plate according to Figure 1a. The result is shown in Figure 4, where the full degree of orientation plots where the data was extracted from can be seen in Figure S5. The inset in Figure 4 of the degree of orientation plot in the CD−TD plane shows that the first layer consisting of shish-kebab structures is slightly thinner in the low viscosity compared to in medium-viscosity LDPE. In addition, the second layer is considerably thicker in medium-viscosity LDPE than in low-viscosity LDPE. Figure 4 shows a clear difference between medium-viscosity LDPE (in red) and low-viscosity LDPE (in blue) in the shear and bulk layers. In medium-viscosity LDPE, the shear layer has a higher degree of orientation, in particular seen in the MD−TD plane. In addition, in medium-viscosity LDPE, the shear layer is thicker, whereas the bulk layer is thinner compared to in low-viscosity LDPE. Overall, low-viscosity LDPE has a lower degree of orientation compared to medium-viscosity LDPE. The difference in viscosity originates from the different molecular weights of the polymer chains, where polymers with higher molecular weights are more viscous. The higher degree of orientation for medium-viscosity LDPE is believed to originate from higher shear rates and longer relaxation times for longer molecules, which would result in less relaxation back to a coiled state, thus resulting in a stronger orientation of molecules during crystallization.

We also investigated the effect of the positions within the injection-molded plate (see Figure 1a, positions 1, 2, and 3). In low-viscosity LDPE, there is no clear difference identified between the positions. In medium-viscosity LDPE, however, there is a significant difference identified, where the most prominent feature is a higher degree of orientation in the shear

https://doi.org/10.1021/acsapm.3c01007
ACS Appl. Polym. Mater. XXXX, XXX, XXX−XXX

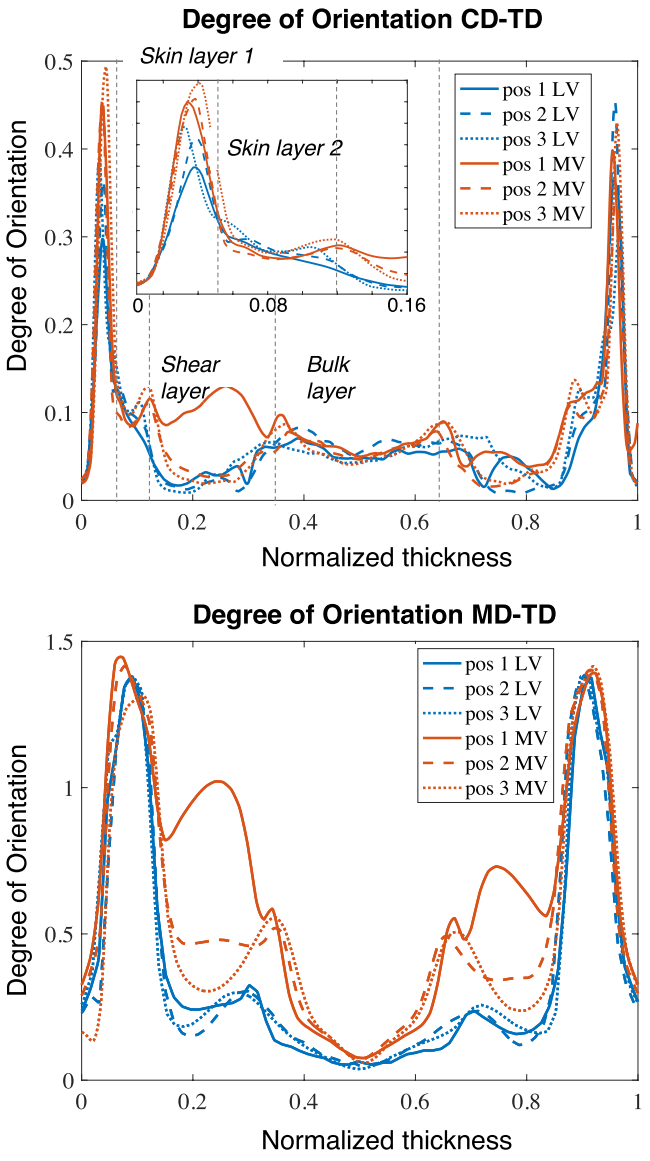

Figure 4. Degree of orientation calculated in CD−TD and MD−TD planes for low-viscosity LDPE (in blue) and medium-viscosity LDPE (in red) for three positions of the injection-molded plate labeled 1, 2, and 3 according to Figure 1a. The inset in the degree of orientation CD−TD shows the distribution of the first and the second layer in higher magnification. The dashed gray lines roughly indicate the start and end of each layer.

layer in position 1, closest to the inlet of the mold. Zuidema et al.[31] described that in injection-molded polypropylene, the thickness of orientated layers decreases with increased distance from the injection gate. The use of scanning SAXS allows us to validate that the thickness of each layer is similar for all positions, but instead the orientation of each layer differs. Also note that all profiles of the degree of orientation presented in Figure 4 are asymmetric horizontally, i.e., with respect to the center of the plate, where for example, the degree of orientation in the shear layer is higher for x = 0.2 compared to x = 0.8. These asymmetries most likely originate from different materials in the two mold tool halves, i.e., steel in the fixed half and aluminum in the movable half. The difference in mold materials results in differences in the cooling rate between the two sides, affecting the overall structure and the degree of orientation of the material.

A correlation function analysis was performed in each layer of both low- and medium-viscosity LDPEs (Figures 5 and S6) to get quantitative values of the degree of crystallinity and lamellae thickness in the different layers of the injection-molded structure. To determine the statistical significance of the results, a MANOVA analysis was performed (Table S2). The skin layers consisting of shish-kebab structures had a significantly higher degree of crystallinity as well as a higher lamellae thickness compared to the shear and bulk layers. Furthermore, a statistically significant difference could be found in lamellae thickness when comparing medium- and low-viscosity LDPEs, where medium-viscosity LDPE gave slightly thicker lamellae. When investigating the effect of the positions within the injection-molded plate (see Figure 1a, positions 1, 2, and 3), no statistically significant difference could be found in lamellae thickness between the different positions, despite the differences observed in the degree of orientation (Figure 4).

The first melting peak of samples collected on various positions of multiple plates produced from low- and medium-viscosity LDPEs was studied by means of DSC in order to study the distribution of melting temperature of the crystalline contents in these positions and hence the distribution of lamellae thickness present in these positions.[32,33] A comparison of the melting endotherms of selected representative samples in each position is presented in Figure S7 in the Supporting Information. The temperature at which the majority of the crystals melted (T_m) is presented in the Supporting Information in Table S3. In agreement with the similar calculated lamella thickness by the correlation function analysis presented in Figure 5, the melt endotherms were similar in all three positions for both LDPE grades, suggesting a similar lamellae thickness in all three positions.

Simulations of the temperature and shear profiles over time are shown for low- and medium-viscosity LDPEs in Figures 6 and 7, respectively. The figures have been assembled by stacking simulated temperature and shear profiles in three positions in time sequences, as described in Figure S4 in the Supporting Information, to represent the different phases of the injection molding process. High shear is present in the injection phase, low shear and high pressure is present in the packing phase, and no shear and low pressure is present in the cooling phase. The blue temperature region in Figure 6 represents the areas where the polymer temperature is below 120 °C. This facilitates the comparison between the materials during crystallization, both at the quiescent crystallization temperature at 100 °C as well as under flow-induced crystallization under shear at higher temperature.[34]

The skin layers (corresponding positions A1, A2, B1, and B2 in Figure 3) are formed as soon the flow front reaches the cold surface of the mold since the mold is cooled by water to 40 °C. The cooling rate at this layer is extremely high, cooling the polymer almost instantaneously under high shear stress and strain from the fountain flow.[1] These conditions provide the prerequisites for flow-induced crystallization of the shish-kebab fiber-like structure as identified in the scattering data. The induced orientation is believed to contribute to the higher crystallinity and thicker lamellae observed in the correlation function analysis (Figure 5). In the shear layer, the next layer toward the center (Figure 3 positions A3 and B3), the material is exposed to more shear-induced heat compared to the skin layers, as seen by the increase of temperature in the polymer (Figure 6). Since this layer will only crystallize during the

https://doi.org/10.1021/acsapm.3c01007
ACS Appl. Polym. Mater. XXXX, XXX, XXX−XXX

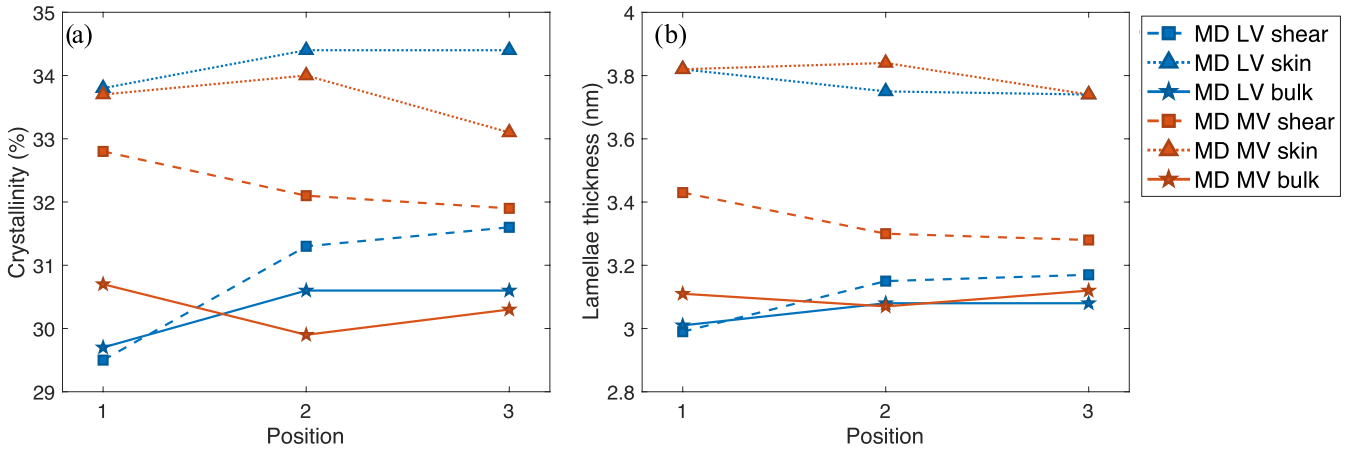

Figure 5. Crystallinity (a) and lamellae thickness (b) calculated for low- and medium-viscosity polyethylene for different layers across the thickness as well as different positions of the injection-molded plate.

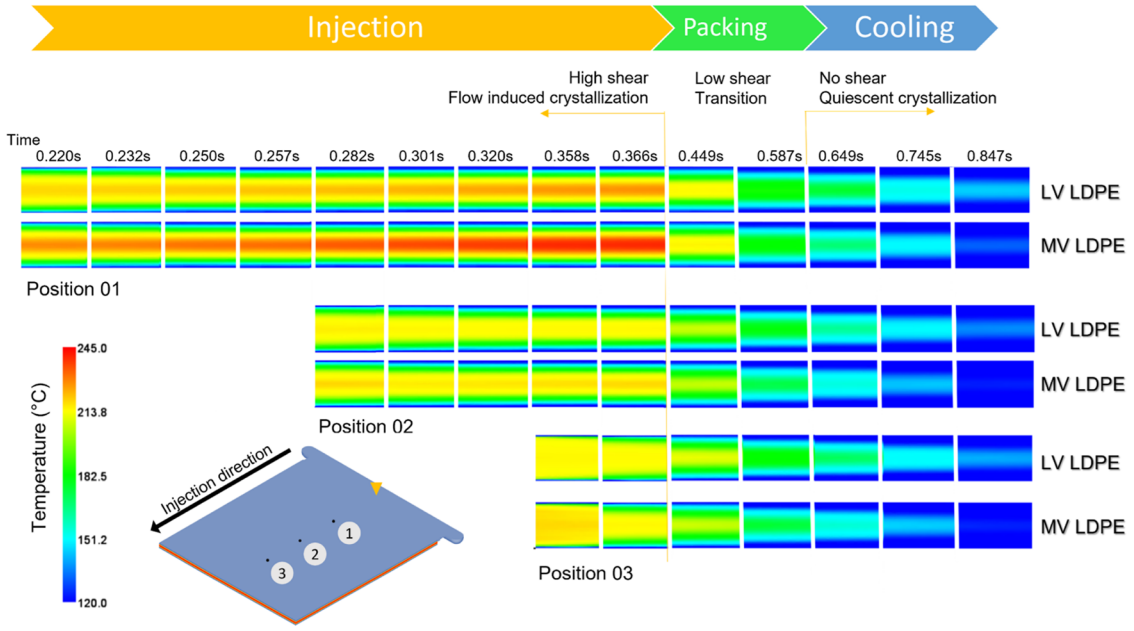

Figure 6. Simulation results of the temperature profile of low- and medium-viscosity LDPEs during injection, packing, and cooling. Observe that the time scale is nonlinear.

packing phase under a lower shear rate, a lower degree of orientation is expected compared to skin layers 1 and 2. The simulation results are thus in agreement with the scattering data, which shows that these layers consist of elongated spherulites.

Even though the temperature when entering the holding pressure phase is higher in the medium-viscosity LDPE than in the low-viscosity LDPE due to more shear-induced heat during the injection phase, the cooling rate is faster due to a lower specific heat, as specified in Table S1. Combined with a higher shear rate and a longer relaxation time for the longer molecules, the induced orientation during the high shear injection phase is more prone to remain before crystallization occurs, resulting in a more anisotropic microstructure. This agrees well with the scanning SAXS results in Figure 4, which show that medium-viscosity LDPE has a thicker shear layer with a higher degree of orientation compared to low-viscosity LDPE.

Crystallization of the bulk layer (Figure 3 position A4 and B4) takes longer time in low-viscosity LDPE than in the medium-viscosity, again due to the higher specific heat (Table S1), providing more time for the polymer chain to relax and form a thicker layer of symmetric spherulites by quiescent crystallization.

The main difference in the results from simulations between the three different positions on the plate is the time duration of the injection phase (Figures 6 and 7), where the polymer melt reaches position 1 significantly earlier than in position 3, resulting in a longer time under shear in position 1 compared with the position further away from the injection point. Also, the shear rates during the injection phase are significantly higher in position 1 compared with the others, which also results in a higher temperature during injection. The higher shear rates combined with a longer time duration in shear during the injection phase enables a stronger orientation of the polymer chains in position 1, which agrees well with the

https://doi.org/10.1021/acsapm.3c01007
ACS Appl. Polym. Mater. XXXX, XXX, XXX−XXX

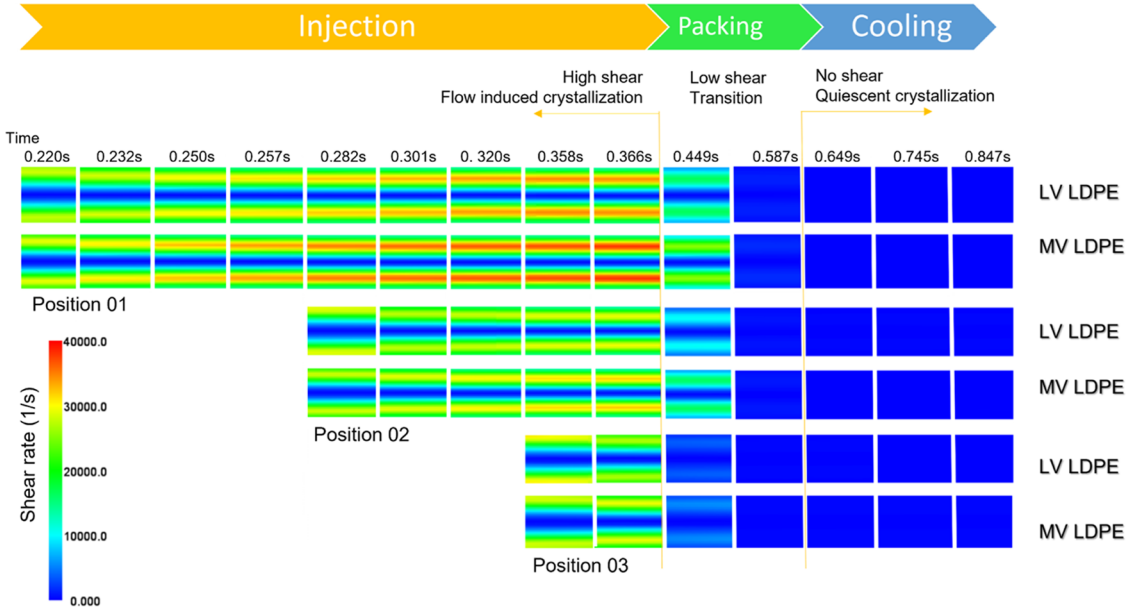

Figure 7. Simulation results of the shear rate profile of low- and medium-viscosity LDPEs during injection, packing, and cooling. Observe that the time scale is nonlinear.

observations in the degree of orientation graphs presented in Figure 4.

The layers identified in Figure 3 refer to medium-viscosity LDPE in position 2, where two distinct layers were identified in the skin (A1, A2, B1, and B2). Considering the temperature and shear rate profiles in Figures 6 and 7 for position 2 and medium-viscosity LDPE, one can identify differences in temperatures and shear profiles in the outermost layers. In the layer identified as skin layer 1, the shear rate is lower during the injection phase, whereas in the layer identified as skin layer 2, the shear rate is higher during the injection phase. With such differences in shear rate, it is likely that both layers contain shish-kebab morphologies, but with a difference in their lamella chain axis orientation, i.e., Keller Machine type I and type II, respectively, with the higher shear rate in skin layer 2 giving rise to Keller Machine type II, with lamellae with a c-axis parallel to the flow.

In order to investigate the influence of structural differences on the mechanical properties of the materials, tensile tests were performed. Figure 8 shows the stress as a function of strain obtained from tensile tests on dogbones from low- and medium-viscosity LDPEs. The curves are averaged curves based on ten samples, and their respective breakpoints are indicated by dots. Both medium- and low-viscosity PEs have a higher ultimate tensile strength when deformed in the MD compared to in the CD. The shish-kebab microstructure is reported to improve the tensile strength of the material in the direction of the fibril-like shish.[35−37] Thus, the difference between material strength in the MD compared to in the CD could be explained by the orientation of the highly oriented shish-kebab microstructure in the skin layer, as well as the oriented elongated spherulites in the shear layer. From Figure 4, it can be seen that low-viscosity LDPE has slightly thinner skin layers as well as less oriented and thinner shear layers compared to medium-viscosity LDPE. The higher tensile strength and higher stiffness observed in medium-viscosity LDPE compared to low-viscosity LDPE could be explained by the difference in thickness of highly oriented layers

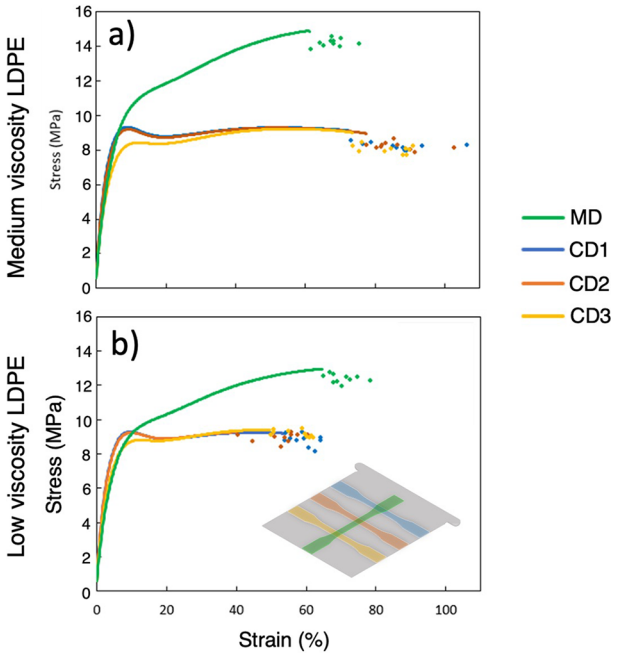

Figure 8. Tensile test of medium-viscosity LDPE (a) and low-viscosity LDPE (b). CD1, CD2, and CD3 denote different positions in CD. The averaged stress−strain curve of 10 samples is shown as a solid line, and the breakpoints for each sample are shown as dots.

In the CD, both low- and medium-viscosity LDPEs have almost identical yield points suggesting that the materials require the same stress to be deformed. However, medium-viscosity LDPE has a higher elongation at break compared to low-viscosity LDPE. While our study does not allow us to validate this result, we hypothesize that the difference originates from their different molecular weights, giving different prerequisites for tie molecules, i.e., polymer chains that are part of more than one crystalline lamellae, which are reported to have a strong influence on the ultimate deformation.[38,39]

https://doi.org/10.1021/acsapm.3c01007
ACS Appl. Polym. Mater. XXXX, XXX, XXX−XXX

For both low- and medium-viscosity LDPEs, the yield points are similar in CD position 1 and CD position 2 while having a significantly lower stress and larger deformation at yield in CD position 3, furthest away from the gate. Notably, the differences between positions identified in the degree of orientation plots from SAXS measurements (as presented in Figure 4) showed that position 1 deviated from positions 2−3. The differences between the observations of the degree of orientation and mechanical response do, however, not necessarily mean a contradiction. The differences between position 1 and positions 2−3 identified by SAXS, i.e., a higher degree of orientation in the shear layer in position 1, would most likely give rise to notable effects on the tensile response when deformed in the MD, while the differences in the tensile response in different positions, as shown in Figure 8 were investigated in the CD. Unfortunately, due to the geometries of the test plate and the dogbone, no such experiments, with the deformation of samples taken from three different positions along the flow path of the test plate, were possible to be performed in the MD. A lower yield strength would suggest thinner lamellae and/or a lower crystallinity, as supported by Schrauwen et al.[6] However, neither the lamellae thickness calculated by correlation analysis function from scanning SAXS in Figure 5 nor DSC results presented in Figure S7 and Table S3 show thinner lamellae or lower crystallinity in position 3 in any of the two LDPEs. The differences in yield strength must then be explained by other factors not covered in our study rather than the degree of orientation or lamellae thickness.

In order to evaluate how the microstructure evolves upon tensile testing and fracture, MD and CD2 dogbones, i.e., samples deformed in the MD and CD, respectively, were measured with scanning SAXS after the fracture (Figure 9). Selected 2D scattering patterns of dogbones in the side view can be seen in Figure S10.

In CD, the dogbone had a clear necking, which was not visible in the MD (Figure 9g). Thus, a larger region of interest was chosen for the dogbone deformed in the CD compared to the MD. Figure 9a shows the asymmetric intensity plot of a top view sample, i.e., the CD−MD plane, deformed in the CD, where the colors represent the main orientation angle of the scattering patterns. The upper part of the image corresponds to the undeformed part of the dogbone. In that region, the scattering patterns are aligned in the horizontal direction, as indicated by the blue color of the color wheel, which corresponds to a long axis preferentially oriented in the flow direction in the sample. Note that close to the edge, no contribution from the lamellae can be observed in the scattering patterns in the CD−TD plane. Thus, in the skin layer, the orientation corresponds to the orientation of the shish (Figure S10a). After tensile testing, the lower deformed part of the sample presents scattering patterns aligned in the vertical direction; thus, the deformed fibrillar structures have a preferred orientation in the direction of the tensile stress. This result shows that the deformation spans from macroscopic to the underlying nanostructure. When measured from above (Figure 9a), each point will yield the scattering from the averaged structure through the layered microstructure in the thickness direction.

The asymmetric intensity plot (Figure 9b) of the dogbone in the side view, i.e., in the CD−TD cutting plane, deformed in the CD direction, shows that the alignment of the skin layer is intact even in the deformed regions. Thus, the orientation of the shish-kebab structure in the skin layers is unchanged when

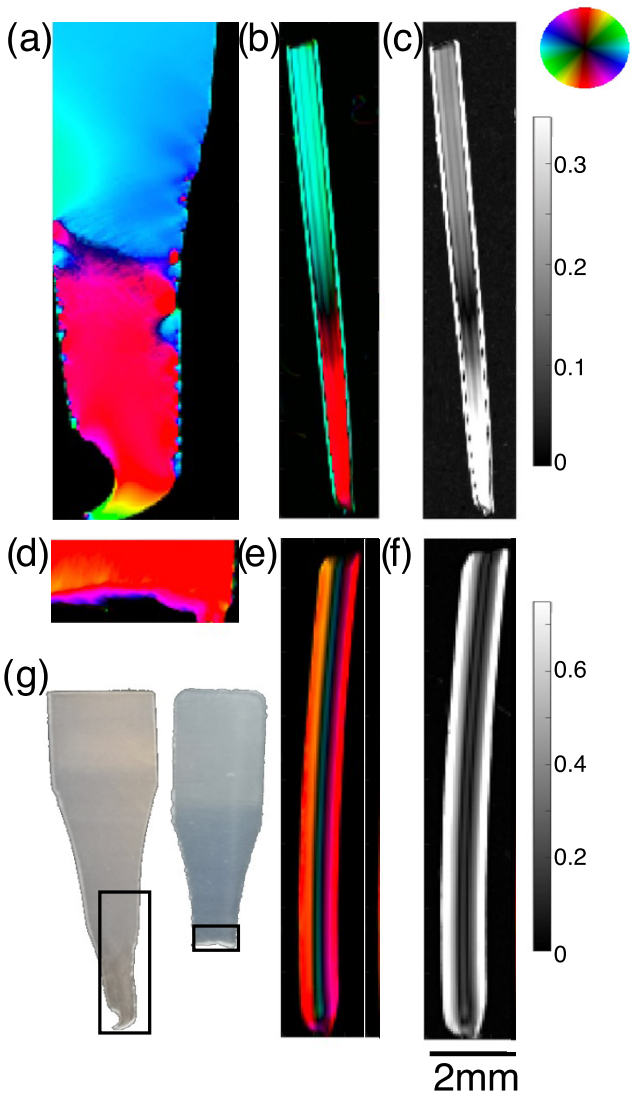

Figure 9. Scanning SAXS of a medium-viscosity LDPE dogbone deformed in CD2 (a−c) and in the MD (d−f), respectively. The asymmetric intensity plot in the top view (a, d) and side view (b, e), as well as the degree of orientation in the side view (c, f). Note the different scaling in the degree of orientation maps. For asymmetric intensity plots, the hue corresponds to the orientation angle of the scattering, whereas the asymmetric scattering corresponds to the value of the color. (g) Photographs of the dogbone-shaped samples deformed in the CD (left) and MD (right). The black rectangles (g) indicate the regions that were measured with scanning SAXS top view (a, d).

tensile stress is applied in the CD. However, the structure of the presumed elongated spherulites of the shear layer changes its orientation, and the randomly oriented spherulites of the bulk layer become orientated in the direction of the applied stress. From Figure 9c, it can also be seen that the degree of orientation in the shear and bulk layers has increased after deformation. In addition, in the deformed region, no contrast between the shear and bulk layer can be seen in the deformed region. Thus, after deformation, the two layers have a similar microstructure, presumably consisting of fibrillar structures in the direction of the stress applied. These observations agree with the results published by Guo et al.,[40] where crystalline segments, formed by a slip of lamellae, beyond the yield point reorient into the direction of the deformation.

https://doi.org/10.1021/acsapm.3c01007
ACS Appl. Polym. Mater. XXXX, XXX, XXX−XXX

Since the dogbone samples deformed in the MD had a very small deformation region, only the very tip was measured in a top view mode. Plots of the asymmetric intensity in the MD top view scan (Figure 9d) show only local variations of orientation close to the fracture surface. Results from the corresponding MD side view scans, i.e., measured in the MD−TD plane (Figure 9e,f), show no change in the orientation angle of the layered structure when approaching the fracture surface. This is in agreement with previous work,[36] where it was hypothesized that the strong shish-kebab structure sustains most of the tensile forces until cracks are formed in the skin layer, breaking the structure promptly.

Figure 10 shows results from peak fitting of the main SAXS peak, which corresponds to the so-called long-spacing, i.e., the

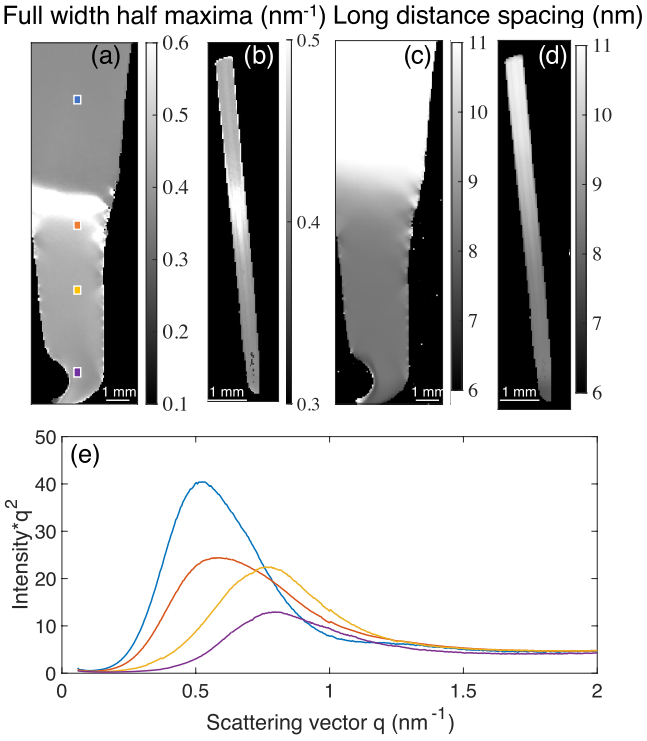

Figure 10. Results from peak fitting of scanning SAXS data of medium-viscosity dogbones deformed in the CD (a−d), as well as azimuthally integrated data for some selected points (e). (a) and (b) Calculated full-width half maxima of the peak across the top view and side view samples, respectively, and (c) and (d) $2*\pi/$(peak position) corresponding to the length of the full-period d-spacing.

thickness of one crystalline and one amorphous layer, of the dogbone deformed in the CD. The top part of the samples corresponds to areas with low deformation, and these areas are characterized by a narrow peak width (Figure 10a,b) as well as a large long spacing (Figure 10c,d). A narrow peak width indicates a relatively low dispersity of the long-distance spacing. In the side view sample (Figure 10b), the peak width is narrowest in the bulk, which is consistent with having a longer cooling time during the injection molding process, enabling more controlled crystallization behavior.

In the deformed parts of the samples, there are noticeable changes in both the peak width and the peak position. First, the peak width becomes broader and the long period taken as $2*\pi/$peak position becomes shorter, as shown in Figure 10a in the area with the orange dot and Figure 10c, respectively. The radially integrated data (Figure 10e) shows that the overall peak intensity has decreased in the deformed region. Taking the shift of the long period, peak width, and peak intensity into account, the results suggest that when deformation starts, large structures are first disrupted, creating new smaller structures. Closer to the fracture position (yellow and purple dots in Figure 10a), the peak width decreases as the long period decreases. This indicates that increasing amounts of the large structures are disrupted, giving rise to structures with smaller, relatively defined long-distance spacing. In addition, the radially integrated data (Figure 10e) shows that the peak intensity consistently decreases closer to the fracture position, consistent with having a decreasing amount of crystalline structures present. Thus, our results suggest that when the sample is deformed in the CD, large structures break apart into smaller structures simultaneously as they reorient in the direction of the applied stress.

CONCLUSIONS

In summary, hierarchical structures of injection-molded LDPE with low and medium viscosities have been investigated using a combination of synchrotron scanning SAXS, numerical FEM simulations, thermal analysis, and tensile testing. It was found that the injection-molded plate specimen consists of four distinct layers with highly oriented shish-kebab structures in two skin layers, intermediately oriented elongated spherulites in the shear layer, and symmetrical spherulites in the bulk layer. The presence of a layered morphology was strengthened by numerical simulations, where high shear and cooling rates explained having more orientated structures closer to the edge compared to the center of the plate thickness, where there were low shear rates and slow cooling. Anisotropic shish-kebab and elongated spherulites are reported to improve mechanical performance in the direction of the flow. The microstructure identified with scanning SAXS and numerical simulations was consistent with the tensile testing result, which showed that the ultimate tensile strength was indeed higher when the samples were deformed in the direction of the flow. The two perpendicular directions were further investigated by using scanning SAXS on deformed samples after the fracture. When deformed perpendicular to the flow, the orientation of the skin layers stays intact, whereas the layers consisting of elongated spherulites and symmetrical spherulites change their orientation in the direction of the applied stress. When instead deformed in the direction of the flow, no change in the orientation can be observed.

When comparing two LDPEs with different viscosities, it was shown that medium-viscosity LDPE exhibited, on average, a higher degree of orientation compared to low-viscosity LDPE. By using numerical simulations, it was concluded that medium viscosity is more prone to forming oriented structures due to having a higher shear rate in combination with a higher cooling rate present during the injection-molded process. As a result of the higher degree of orientation, medium-viscosity LDPE showed a higher tensile strength when deformed in the direction of the flow.

It was further shown that the distance from the injection gate influences the structures formed, where a higher degree of orientation was observed closer to the gate of the mold. By using simulation results, we concluded that the main difference seen in the scattering data is due to having a longer time under shear as well as a higher shear rate closer to the injection gate.

https://doi.org/10.1021/acsapm.3c01007
ACS Appl. Polym. Mater. XXXX, XXX, XXX−XXX

■ ASSOCIATED CONTENT

Supporting Information

The Supporting Information is available free of charge at https://pubs.acs.org/doi/10.1021/acsapm.3c01007.

Finite element model, input data, and methods for the injection molding simulations; examples of the peak-fitting procedure and correlation function analysis of SAXS data; scanning SAXS degree of orientation and DSC measurements of different positions of the injection-molded plate for both low- and medium-viscosity LDPEs; MANOVA statistical analysis and the long-distance period from SAXS correlation function analysis; radially integrated SAXS data for positions A1-4 in Figure 3; WAXS measurements of medium-viscosity LDPE; and selected 2D scattering patterns of the medium-viscosity LDPE dogbones and cross section; and beam profile of the X-ray beam (PDF)

■ AUTHOR INFORMATION

Corresponding Author

Marianne Liebi − *Department of Physics, Chalmers University of Technology, 412 96 Gothenburg, Sweden; Paul Scherrer Institute, 5232 Villigen PSI, Switzerland; Institute of Materials, Ecole Polytechnique Fédérale de Lausanne (EPFL), 1015 Lausanne, Switzerland;* orcid.org/0000-0002-5403-0593; Email: Marianne.liebi@psi.ch

Authors

Linnea Björn − *Department of Physics, Chalmers University of Technology, 412 96 Gothenburg, Sweden; FibRe-Centre for Lignocellulose-Based Thermoplastics, Department of Chemistry and Chemical Engineering, Chalmers University of Technology, 412 96 Gothenburg, Sweden;* orcid.org/0000-0001-8153-2129

Renan Melhado Mazza − *Tetra Pak, 221 86 Lund, Sweden;* orcid.org/0009-0002-8463-8062

Eskil Andreasson − *Tetra Pak, 221 86 Lund, Sweden;* orcid.org/0000-0001-8325-9226

Fredrik Linell − *Tetra Pak, 221 86 Lund, Sweden;* orcid.org/0009-0007-3817-9121

Viviane Lutz-Bueno − *Paul Scherrer Institute, 5232 Villigen PSI, Switzerland*

Manuel Guizar-Sicairos − *Paul Scherrer Institute, 5232 Villigen PSI, Switzerland*

Elin Persson Jutemar − *Tetra Pak, 221 86 Lund, Sweden;* orcid.org/0000-0002-9076-1385

Complete contact information is available at: https://pubs.acs.org/10.1021/acsapm.3c01007

Funding

LB has been supported by the Swedish Innovation Agency VINNOVA 2019-02563 and FibRe, a VINNOVA competence center. ML acknowledges funding from the Area of Advance Material Science at Chalmers University of Technology. This work was supported by the Chalmers Gender Initiative for Excellence (Genie).

Notes

The authors declare no competing financial interest.

■ ACKNOWLEDGMENTS

The authors acknowledge the Paul Scherrer Institute, Villigen PSI, Switzerland, for the provision of the synchrotron radiation beamtime at the beamline cSAXS of the SLS. Daniela Nae is acknowledged for the help provided during sample preparation.

■ REFERENCES

(1) Kantz, M. R.; Newman, H. D.; Stigale, F. H. The skin-core morphology and structure−property relationships in injection-molded polypropylene. *J. Appl. Polym. Sci.* **1972**, *16*, 1249−1260.

(2) Schrauwen, B. A. G.; Govaert, L. E.; Peters, G. W. M.; Meijer, H. E. H. The influence of flow-induced crystallization on the impact toughness of high-density polyethylene. *Macromol. Symp.* **2002**, *185*, 89−102.

(3) Liu, X. H.; Zheng, G. Q.; Jia, Z. H.; Li, S. W.; Liu, C. G.; Zhang, Y.; Shao, C. G.; Shao, C.; Dai, K.; Dai, K.; Liu, B. C.; Liu, B.; Zhang, Q. X.; Zhang, Q.; Wang, S. J.; Wang, S.; Liu, C.; Liu, C.; Chen, J. B.; Chen, J.; Peng, X. F.; Peng, X.; Shen, C. Y. The hierarchical structure of water-assisted injection molded high density polyethylene: Small angle X-ray scattering study. *J. Appl. Polym. Sci.* **2012**, *125*, 2297−2303.

(4) Wang, L.; Wang, J. H.; Yang, J. H.; Yang, B.; Wang, B.; Wang, Y.; Zhang, Q. P.; Zhang, Q. P.; Yang, M. B.; Yang, M. B.; Feng, J. M. A novel hierarchical crystalline structure of injection-molded bars of linear polymer: co-existence of bending and normal shish-kebab structure. *Colloid Polym. Sci.* **2013**, *291*, 1503−1511.

(5) Bartczak, Z.; Vozniak, A. WAXS/SAXS study of plastic deformation instabilities and lamellae fragmentation in polyethylene. *Polymer* **2019**, *177*, 160−177.

(6) Schrauwen, B. A. G.; Janssen, R. P. M.; Govaert, L. E.; Meijer, H. E. H. Intrinsic Deformation Behavior of Semicrystalline Polymers. *Macromolecules* **2004**, *37*, 6069−6078.

(7) Schrauwen, B. A. G.; Breemen, L. C. A.; Spoelstra, A. B.; Govaert, L. E.; Peters, G. W. M.; Meijer, H. E. H. Structure, Deformation, and Failure of Flow-Oriented Semicrystalline Polymers. *Macromolecules* **2004**, *37*, 8618−8633.

(8) Deng, B.; Chen, L.; Li, X.; Wang, Z. B. Influence of Prereserved Shish Crystals on the Structural Evolution of Ultrahigh-Molecular Weight Polyethylene Films during the Hot Stretching Process. *Macromolecules* **2022**, *55*, 4600−4613.

(9) Keller, A.; Machin, M. J. Oriented crystallization in polymers. *J. Macromol. Sci., Part B: Phys.* **1967**, *1*, 41−91.

(10) Zhou, H. *Computer Modeling for Injection Molding: Simulation, Optimization, and Control*; Wiley: New Jersey, 2013; p 197.

(11) Horváth, Z.; Menyhárd, A.; Doshev, P.; Gahleitner, M.; Kock, C.; Kheirandish, S.; Varga, J.; Pukánszky, B. Effect of molecular architecture on the crystalline structure and stiffness of iPP homopolymers: Modeling based on annealing experiments. *J. Appl. Polym. Sci.* **2013**, *130*, 3365−3373.

(12) Martinez De Salazar, J.; BaltáCalleja, F. J. Influence of chain defects on the crystallization of polyethylene with reference to crystal size and perfection. *J. Cryst. Growth* **1980**, *48*, 283−294.

(13) Somani, R. H.; Yang, L.; Hsiao, B. S. Effects of high molecular weight species on shear-induced orientation and crystallization of isotactic polypropylene. *Polymer* **2006**, *47*, 5657−5668.

(14) Wang, Z. B.; Mao, Y. M.; Li, X. K.; Li, Y. G.; Jarumaneeroj, C.; Thitisak, B.; Tiyapiboonchaiya, P.; Rungswang, W.; Hsiao, B. S. The Influence of Ethyl Branch on Formation of Shish-Kebab Crystals in Bimodal Polyethylene under Shear at Low Temperature. *Chin. J. Polym. Sci.* **2021**, *39*, 1050−1058.

(15) Wang, Z.; Zhu, M.; Song, T.; Li, X.; Hsiao, B. S. Shear-induced crystallization of unimodal/bimodal polyethylene at high temperatures affected by C4 short-branching. *Polymer* **2021**, *233*, No. 124203.

(16) Cao, W.; Wang, K.; Zhang, Q.; Du, R.; Fu, Q. The hierarchy structure and orientation of high density polyethylene obtained via dynamic packing injection molding. "The overall orientation in the molded bar increased with decreased MFI". *Polymer* **2006**, *47*, 6857−6867.

(17) Liu, X.; Zhang, C. G.; Dai, K.; Zheng, G. Q.; Liu, C.; Shen, C. Unexpected molecular weight dependence of shish kebab in water-assisted injection molded HDPE. *Polym. Adv. Technol.* **2013**, *24*, 270−272.
(18) Tan, V.; Kamal, M. R. Morphological Zones and Orientation in Injection-Molded Polyethylene. *J. Appl. Polym. Sci.* **1978**, *22*, 2341−2355.
(19) Leo, V.; Cuvelliez, C. The Effect of the Packing Parameters, Gate Geometry, and Mold Elasticity on the Final Dimensions of a Molded Part. *Polym. Eng. Sci.* **1996**, *36*, 1961−1971.
(20) Zheng, R.; Tanner, R.; Wo, D. L.; Fan, X. J.; Hadinata, C.; Costa, F.; Kennedy, P.; Zhu, P.; Edward, G. H. Modeling of flow-induced crystallization of colored polypropylene in injection molding. *Korea Aust. Rheol. J.* **2010**, *22*, 151−162.
(21) Tosello, G.; Costa, F. S. High precision validation of micro injection molding process simulations. *J. Manuf. Process.* **2019**, *48*, 236−248.
(22) Speranza, V.; Liparoti, S.; Panani, R.; Titomanlio, T. Prediction of morphology development within micro-injection molding samples. *Polymer* **2021**, *228*, No. 123850.
(23) Henrich, B.; Bergamaschi, A.; Broennimann, C.; Dinapoli, R.; Eikenberry, E. F.; Johnson, I.; Kobas, M.; Kraft, P.; Kraft, P.; Mozzanica, A.; Mozzanica, A.; Schmitt, B. PILATUS: A single photon counting pixel detector for X-ray applications. *Nucl. Instrum. Methods Phys. Res., Sect. A* **2009**, *607*, 247−249.
(24) Bunk, O.; Bech, M.; Jensen, T. H.; Feidenhans, R.; Binderup, T.; Menzel, A.; Pfeiffer, F. Multimodal x-ray scatter imaging. *New J. Phys.* **2009**, *11*, No. 123016.
(25) Strobl, G. R.; Schneider, M. Direct evaluation of the electron density correlation function of partially crystalline polymers. *J. Polym. Sci., Polym. Phys. Ed.* **1980**, *18*, 1343−1359.
(26) Ruland, W. The evaluation of the small-angle scattering of lamellar two-phase systems by means of interface distribution functions. *Colloid Polym. Sci.* **1977**, *255*, 417−427.
(27) Ferri, D.; Perolo, A.; Nodari, M. Cross-WLF parameters to predict rheological properties of polylactic acid. *Annu. Trans. Nord. Rheol. Soc.* **2017**, *25*, 419−426.
(28) Keum, J. K.; Burger, C.; Zuo, F.; Hsiao, B. Probing nucleation and growth behavior of twisted kebabs from shish scaffold in sheared polyethylene melts by in situ X-ray studies. *Polymer* **2007**, *48*, 4511−4519.
(29) Bartczak, Z.; Vozniak, A. Microbuckling Instability and the Second Yield during the Deformation of Semicrystalline Polyethylene. *Polymers* **2020**, *12*, 2208.
(30) Katti, S. S.; Schultz, M. The Microstructure of Injection-Molded Semicrystalline Polymers: A Review. *Polym. Eng. Sci.* **1982**, *22*, 1001−1017.
(31) Zuidema, H.; Peters, G. W. M.; Meijer, H. E. H. Development and Validation of a Recoverable Strain-Based Model for Flow-Induced Crystallization of Polymers. *Macromol. Theory Simul.* **2001**, *10*, 447−460.
(32) Hoffman, J. D.; Davis, G. T.; Lauritzen, J. I., Jr. *Treatise on Solid State Chemistry Volume 3 Crystalline and Noncrystalline Solids*; Plenum Press: New York, 1976; pp 497−614.
(33) Perez, S. Macromolecular physics. Vol. 3. Crystal melting by B. Wunderlich. *Acta Crystallogr., Sect. A: Cryst. Phys., Diffr., Theor. Gen. Crystallogr.* **1981**, *37*, 606.
(34) Derakhshandeh, M.; Hatzikiriakos, S. G. Flow-induced crystallization of high-density polyethylene: The effects of shear and uniaxial extension. *Rheol. Acta* **2012**, *51*, 315−327.
(35) Jiang, J.; Liu, X.; Lian, M.; Pan, Y.; Chen, Q.; Liu, H.; Zheng, G. Q.; Guo, Z.; Schubert, D. W.; Shen, C.; Liu, C. Self-reinforcing and toughening isotactic polypropylene via melt sequential injection molding. *Polym. Test.* **2018**, *67*, 183−189.
(36) Mi, D.; Zhou, M.; Zhang, J. Quantification of shish−kebab and ß-crystal on the mechanicalproperties of polypropylene. *J. Appl. Polym. Sci.* **2017**, *134*, 45052.
(37) Zhou, M.; Li, X. P.; Jin, M.; Xia, C.; Shen, K. Z.; Zhang, J. Simultaneously, improving the tensile and impact properties of isotactic polypropylene with the cooperation of co-PP and β-nucleating agent through pressure vibration injection molding. *Chin. J. Polym. Sci.* **2016**, *34*, 1001−1013.
(38) Kida, T.; Hiejima, Y.; Nitta, K. H.; Yamaguchi, M. Evaluation of microscopic structural changes during strain hardening of polyethylene solids using In situ Raman, SAXS, and WAXD measurements under step-cycle test. *Polymer* **2022**, *250*, No. 124869.
(39) Kennedy, M. A.; Peacock, A. J.; Mandelkern, L. Tensile Properties of Crystalline Polymers: Linear Polyethylene. *Macromolecules* **1994**, *27*, 5297−5310.
(40) Guo, H.; Rinaldi, R. G.; Broudin, M.; Tayakout, S.; Lame, O. Anisotropic deformation and failure behaviors of the necked HDPE materials induced by oligo-cyclic loading. *Polymer* **2021**, *234*, No. 124232.

https://doi.org/10.1021/acsapm.3c01007
ACS Appl. Polym. Mater. XXXX, XXX, XXX−XXX